

Compressed Sensing MRI Using Discrete Nonseparable Shearlet Transform and FISTA

Slavche Pejovski, Venceslav Kafedziski, *Senior Member, IEEE*, and Dušan Gleich, *Member, IEEE*

Abstract—We propose a new compressed sensing MRI approach that uses the discrete nonseparable shearlet transform (DNST) as a sparsifying transform and the fast iterative soft thresholding algorithm (FISTA) for reconstruction. FISTA has a simple design and has shown good convergence behavior. The DNST transform has excellent localization properties within the space domain and excellent directional selectivity. We utilize the frequency representation of the DNST canonical dual filters to obtain a memory efficient modified FISTA based algorithm with a simple and efficient way of calculating the update, tuned to the non tight frame DNST transform. The proposed approach shows improved performance and similar execution time when compared with other state of the art reconstruction approaches.

Index Terms—Compressed sensing, discrete nonseparable shearlet transform (DNST), FISTA, MRI.

I. INTRODUCTION

IN APPLICATIONS where the signal can be efficiently represented using a few significant components, compressed sensing (CS) allows for good reconstruction even when the signal is significantly subsampled compared to the Nyquist sampling, necessary for the traditional reconstruction. CS theory and applications are a field of active research [1], [2]. One area where CS is highly applicable is the magnetic resonance imaging (MRI). It is a noninvasive diagnostic technique widely used in modern medicine. The use of CS in MRI reduces the number of samples and the time needed to obtain the MRI scan [3]. Namely, the MRI image can be represented using a suitable sparsifying transform, and can be correctly reconstructed using fewer samples in the so called k-space (Fourier domain) than the number of pixels in the image.

In order to improve the performance of the reconstructed image, current trends in CS MRI focus on learning the dictionary of the sparsifying transform [4] or finding a suitable combination of sparsifying transforms with total variation (TV) or TV-like transforms [5]–[9]. The combination of two or more sparsifying transforms is conveniently implemented using analysis based reconstruction algorithms, such as the

Split Bregman Reconstruction Algorithm (SBRA) [6]–[8] and the Alternating Direction of Multipliers algorithms [9]. The use of multiple transforms leads to a number of regularization parameters and increases the algorithm complexity. Here, we use for the first time the Discrete Nonseparable Shearlet Transform (DNST) [10] as a sparsifying transform in MRI. DNST is a compactly supported shearlet transform having excellent localization properties in the spatial domain (creating advantage over the band-limited shearlet transform [11], [12]) and excellent directional selectivity (improving over the contourlets and separable compactly supported shearlets [10]). The DNST uses doubly block circulant matrices for calculating the transform coefficients. These matrices can be diagonalized using the 2D DFT which allows for a simple realization of the update routine in each iteration of the reconstruction algorithm. In order to achieve fast convergence of the reconstruction we use the Fast Iterative Soft Thresholding Algorithm (FISTA) [13], [14] which is simple, has a well understood behavior and a good convergence rate of $\mathcal{O}(1/k^2)$ in terms of the number of iterations k . In order to reduce the memory requirements, which is a major issue for DNST, we modify the FISTA algorithm to use the 2D DFT of the spatial form in the acceleration and update substeps. This is the first work in the MRI literature to combine FISTA and shearlets. Bandlimited shearlet transforms have been previously used in MRI [6]–[8] but they have inferior localization properties compared to DNST, which has not been used in MRI so far. Additionally, these authors use analysis solutions based on the SBRA ([6], [7] also include diagonalization of circulant matrices), while here we use a synthesis solution based on the proximal gradient. The proposed approach can be also related to [14], but we use DNST instead of contourlets and give a detailed description of the substeps for implementing the modified FISTA based algorithm (which deviates from the usual form for tight frames) and detailed analysis of its complexity that is not the case in [14]. We compare the performance of the proposed approach with that of other state of the art CS MRI approaches and quantify the influence of the different reasons for improved performance. The novelty of our work comes from introducing DNST to CS MRI, combining shearlets and FISTA in CS MRI, and modifying the FISTA algorithm to suit the non tight frame DNST transform.

The proposed approach is described in the following section and performance comparisons to other approaches are shown in Section III, followed by a conclusion.

II. APPROACH DESCRIPTION

Shearlet transforms are very efficient in capturing edges and other anisotropic features in images. 2D Discrete shearlet transform is usually obtained using a cone adapted Discrete Shearlet System (DSS) defined by scaling and shearlet functions ϕ_m , $\psi_{j,k,m}$ and $\tilde{\psi}_{j,k,m}$, generated by a scaling generator $\phi \in L^2(\mathbb{R}^2)$

Manuscript received November 28, 2014; revised February 18, 2015; accepted March 03, 2015. Date of publication March 18, 2015; date of current version March 25, 2015. The associate editor coordinating the review of this manuscript and approving it for publication was Prof. Chandra Sekhar Seelamantula.

S. Pejovski and V. Kafedziski are with the Faculty of Electrical Engineering and Information Technologies, University Ss. Cyril and Methodius, Skopje, Republic of Macedonia (e-mail: slavchep@feit.ukim.edu.mk; kafedzi@feit.ukim.edu.mk).

D. Gleich is with the Faculty of Electrical Engineering and Computer Science, University of Maribor, Maribor, Slovenia (e-mail: dusan.gleich@uni-mb.si).

Color versions of one or more of the figures in this paper are available online at <http://ieeexplore.ieee.org>.

Digital Object Identifier 10.1109/LSP.2015.2414443

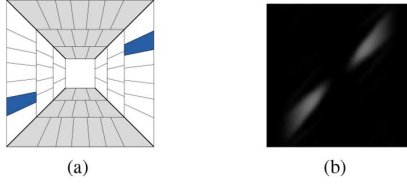


Fig. 1. (a) Frequency tiling by a cone adapted discrete shearlet system for an ideal bandlimited DST, each shearlet function has two symmetric tiles e.g. the blue tiles (b) Frequency tiles corresponding to a single DNST filter.

parameterized by translation parameter m , and shearlet generators $\psi \in L^2(\mathbb{R}^2)$ and $\tilde{\psi} \in L^2(\mathbb{R}^2)$ parameterized by scaling parameter j , translation parameter m and shear (direction) parameter k :

$$\{\phi_m : m \in \mathbb{Z}^2\} \cup \left\{ \psi_{j,k,m}, \tilde{\psi}_{j,k,m} : j \in \mathbb{Z}, j \geq 0; k \in \mathbb{Z}, |k| \leq 2^{\lceil \frac{j}{2} \rceil}; m \in \mathbb{Z}^2 \right\}$$

where $\tilde{\psi}_{j,k,m}$ is obtained from $\psi_{j,k,m}$ by swapping the two variables. The frequency tiling induced by such DSS is shown in Fig. 1(a), where ϕ_m , $\psi_{j,k,m}$ and $\tilde{\psi}_{j,k,m}$ are associated with the square in the center, the horizontal cone (brighter) and the vertical cone, respectively. Each scale corresponds to a ring of tiles and a shear is associated with a pair of tiles in a certain direction within the ring. For DNST, ψ is constructed from a separable compactly supported shearlet generator (excellent localization properties) and a 2D nonseparable fan filter (improved directional selectivity). We denote the digital shearlet filters which discretize ϕ_m , $\psi_{j,k,m}$ and $\tilde{\psi}_{j,k,m}$ by ϕ^d , $\psi_{j,k}^d$, $\tilde{\psi}_{j,k}^d \in \ell^2(\mathbb{Z}^2)$ [10]. With a proper choice of the parameters associated with the translation, the DNST is obtained as a series of filtering operations by ϕ^d , $\tilde{\psi}_{j,k}^d$, $\psi_{j,k}^d$ applied to the 2D discrete signal, where $\bar{z}(n) = z(-n)$ for $n \in \mathbb{Z}^2$. The magnitude of 2D DFT of such a filter is shown in Fig. 1(b). We use the notation h_i to represent any of ϕ^d , $\psi_{j,k}^d$, $\tilde{\psi}_{j,k}^d$, $i = 1, \dots, I$, where I is equal to the total number of shears at different scales plus one.

For mathematical purposes, the MRI image $x(m, n)$ of dimension $\sqrt{N} \times \sqrt{N}$, can be represented as a $N \times 1$ vector \mathbf{x} obtained by stacking the columns (vectorizing) of the image matrix. The MRI scan contains the 2D DFT $X(k, l)$ of $x(m, n)$. By vectorizing $X(k, l)$ we obtain $\tilde{\mathbf{X}}$. In matrix notation we have $\tilde{\mathbf{X}} = \mathcal{F}\mathbf{x}$, where $\mathcal{F} = F \otimes F$ is an $N \times N$ matrix, F is the $\sqrt{N} \times \sqrt{N}$ DFT matrix and \otimes denotes the Kronecker product. The DNST allows for sparse representation of \mathbf{x}

$$\mathbf{s} = \Psi \mathbf{x} \quad (1)$$

where \mathbf{s} is a $U \times 1$ vector ($U = IN$) containing a small number of significant components and Ψ is a $U \times N$ DNST analysis frame matrix operator. In our case $\Psi = [\Psi_1^T, \Psi_2^T, \dots, \Psi_I^T]^T$, where Ψ_i is an $N \times N$ doubly block circulant matrix obtained in terms of \tilde{h}_i , $i = 1, \dots, I$. Thus, Ψ_i can be diagonalized using \mathcal{F} as $\Psi_i = \mathcal{F}^{-1} \Lambda_i \mathcal{F}$. Introducing $\mathbf{s}_i = \Psi_i \mathbf{x}$, we have $\hat{\mathbf{S}}_i = \hat{\mathbf{H}}_i^* \odot \tilde{\mathbf{X}}$, where $\hat{\mathbf{S}}_i = \mathcal{F} \mathbf{s}_i$ and $\hat{\mathbf{H}}_i = \mathcal{F} \mathbf{h}_i$ (\mathbf{h}_i is the vectorized h_i), \odot is the element-wise product, and $*$ denotes conjugate. Introducing Ψ_r , the $N \times U$ frame matrix operator dual to Ψ , we obtain the synthesis equation $\mathbf{x} = \Psi_r \mathbf{s} = \Psi_r \Psi \mathbf{x}$. Ψ_r consists of Ψ_{r_i} for $i = 1, \dots, I$, such that $\Psi_r = [\Psi_{r_1}, \dots, \Psi_{r_I}]$, where Ψ_{r_i} is associated with the filter h_{r_i} , the dual of h_i . Then, the synthesis is obtained as $\mathbf{x} = \sum_{i=1}^I \Psi_{r_i} \mathbf{s}_i$, or $\tilde{\mathbf{X}} = \mathcal{F} \Psi_r \mathbf{s} = \sum_{i=1}^I \hat{\mathbf{H}}_{r_i} \odot \hat{\mathbf{S}}_i$. $\hat{\mathbf{H}}_{r_i}$ are evaluated as $\hat{\mathbf{H}}_{r_i} = \mathcal{F} \mathbf{h}_{r_i} = \hat{\mathbf{H}}_i \odot \hat{\mathbf{G}}$, where \mathbf{h}_{r_i} is the vectorized h_{r_i} , $\hat{\mathbf{G}} = \sum_{i=1}^I \hat{\mathbf{H}}_i^* \odot \hat{\mathbf{H}}_i$, and \odot is an element-wise division.

Input : The Lipschitz constant L of ∇f_2 , number of iterations K , constant λ

Step 0 : Set $\mathbf{r}^1 = \mathbf{s}^0$, $t^1 = 1$

Step k : ($k \geq 1$)

$$\mathbf{u}^k = \mathbf{r}^k - \frac{1}{L} \nabla f_2(\mathbf{r}^k) = \mathbf{r}^k - \frac{1}{L} \mathbf{A}^H \mathbf{A} \mathbf{r}^k + \frac{1}{L} \mathbf{A}^H \mathbf{y} \quad (6)$$

$$\mathbf{s}^k = \text{prox}_{\frac{1}{L} f_1}(\mathbf{u}^k) = \min_{\mathbf{z}} \left\{ \frac{1}{L} f_1(\mathbf{z}) + \frac{1}{2} \|\mathbf{z} - \mathbf{u}^k\|_2^2 \right\} \quad (7)$$

$$t^{k+1} = \frac{1 + \sqrt{1 + 4(t^k)^2}}{2}$$

$$\mathbf{r}^{k+1} = \mathbf{s}^k + \left(\frac{t^k - 1}{t^{k+1}} \right) (\mathbf{s}^k - \mathbf{s}^{k-1}) \quad (8)$$

$$\mathbf{s}^{k-1} = \mathbf{s}^k$$

Fig. 2. FISTA algorithm.

The subsampling in CS MRI is carried out by setting some of the values of $\tilde{\mathbf{X}}$ to 0, i.e. by element-wise multiplication of $\tilde{\mathbf{X}}$ with a mask \mathbf{M} , followed by a reduction of the vector components to the number of acquired samples M . The two operations together with \mathcal{F} , used to obtain $\tilde{\mathbf{X}}$ from \mathbf{x} , are represented by the sampling matrix Φ . The acquired signal in the presence of noise becomes:

$$\mathbf{y} = \Phi \mathbf{x} + \mathbf{v} \quad (2)$$

where \mathbf{v} is an $M \times 1$ vector containing the noise samples. Under certain conditions, the sparse vector \mathbf{s} can be correctly reconstructed (if M is sufficiently large) by solving the optimization problem within the CS framework:

$$\min_{\mathbf{s}} \lambda \|\mathbf{s}\|_1 + \frac{1}{2} \|\mathbf{y} - \Phi \Psi_r \mathbf{s}\|_2^2 \quad (3)$$

where $\|\mathbf{s}\|_1 = \sum_{l=1}^U |s_l|$, $\|\cdot\|_2$ is a vector ℓ_2 norm and the constant λ is a parameter that balances the importance of the sparseness of the solution represented by its ℓ_1 norm, and the approximation error given by $\|\mathbf{y} - \Phi \Psi_r \mathbf{s}\|_2^2$. It is known that λ is strongly correlated with the variance of the noise and the sparseness of the true \mathbf{s} , but its value cannot be explicitly computed and is usually considered to be a tuning parameter.

For easier manipulation (3) can be rewritten as:

$$\min_{\mathbf{s}} \lambda \|\mathbf{s}\|_1 + \frac{1}{2} \|\mathbf{y} - \mathbf{A} \mathbf{s}\|_2^2 = \min_{\mathbf{s}} f_1(\mathbf{s}) + f_2(\mathbf{s}) \quad (4)$$

where $f_1(\mathbf{s}) = \lambda \|\mathbf{s}\|_1$ and $f_2(\mathbf{s}) = \frac{1}{2} \|\mathbf{y} - \mathbf{A} \mathbf{s}\|_2^2$ and $\mathbf{A} = \Phi \Psi_r$. The FISTA algorithm that solves (4) using a constant step is given in [13] and is outlined in Fig. 2.

Since $f_1(\mathbf{z}) = \lambda \|\mathbf{z}\|_1$, the proximity substep (7) has a closed form solution [13] which is the soft thresholding with thresholding level $\beta = \frac{\lambda}{L}$. The soft thresholding function $\mathcal{T}_\beta(\mathbf{z})$ is applied component wise:

$$p_i = \mathcal{T}_\beta(z_i) = \begin{cases} \frac{z_i}{|z_i|} (|z_i| - \beta) & |z_i| > \beta \\ 0 & |z_i| \leq \beta \end{cases} \quad (5)$$

The number of subbands I is usually between 20 and 50, and, thus, the memory requirement of the algorithm in Fig. 2 is very high, especially since both \mathbf{s}^k and \mathbf{s}^{k-1} are required for the acceleration in (8). The algorithm requires minimum $(2I+3)N+1$ complex memory locations, not including the memory locations for the filters $\hat{\mathbf{H}}_{r_i}$ and $\hat{\mathbf{H}}_i$ (each of the two groups of filters requires IN complex memory locations). To reduce the memory requirement we modify the algorithm by multiplying (6) and (8) with $\mathcal{F} \Psi_r$. Multiplying (6) by $\mathcal{F} \Psi_r$ and using the definition of \mathbf{A} and the properties of doubly block circulant matrices, we obtain the $N \times 1$ vector $\tilde{\mathbf{D}}^k$ as in (9), shown at the bottom of the next page, where the factor $\hat{\mathbf{G}}$ appears as a consequence of DNST not being a tight frame. In (9) (a) we used the properties of the MRI sampling process and introduced $\hat{\mathbf{Y}} = \mathcal{F} \Phi^H \mathbf{y}$, in

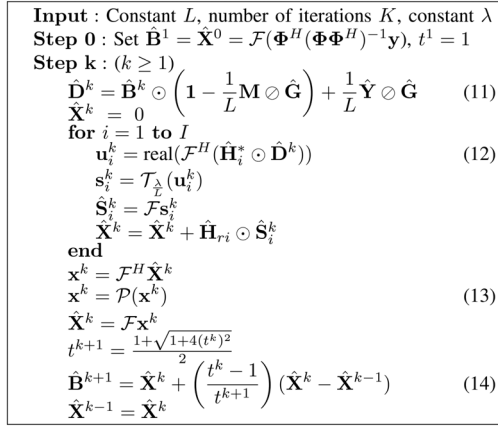


Fig. 3. The Fast discrete Nonseparable Shearlet transform Iterative Soft Thresholding Reconstruction Algorithm (FNSISTRA).

(9) (b) we used $\mathcal{F}\Psi_r \mathbf{r}^k = \sum_{i=1}^I \hat{\mathbf{H}}_{ri} \odot \hat{\mathbf{R}}_i^k$ and in (9) (c) we used $\hat{\mathbf{B}}^k = \sum_{i=1}^I \hat{\mathbf{H}}_{ri} \odot \hat{\mathbf{R}}_i^k$, where $\hat{\mathbf{R}}_i^k = \mathcal{F}\mathbf{r}_i^k$. The multiplication of (8) with $\mathcal{F}\Psi_r$ is evaluated in a similar fashion. The outline of the modified algorithm (termed FNSISTRA) is shown in Fig. 3.

As explained in [8], due to the presence of noise and the subsampling, imaginary components may appear in the solution, degrading the quality of the reconstructed image. To remove this effect, we use the fact that DNST does not introduce an imaginary part if such is absent in the original signal, and we restrict \mathbf{u}^k to real values by (12). Additionally, the values of the reconstructed image must be within a predefined range, and, before applying (14), we keep the real parts of \mathbf{x}^k and project them on the interval $[0, 1]$ as explained in [14], [15]. The projection function in (13) is applied component-wise

$$\mathcal{P}(z_i) = \begin{cases} \text{real}(z_i) & 0 \leq \text{real}(z_i) \leq 1 \\ 0 & \text{real}(z_i) < 0 \\ 1 & 1 < \text{real}(z_i) \end{cases} \quad (10)$$

and requires an additional 2D IDFT and 2D DFT. Without the projections in (12) and (13) and the multiplication with $\mathcal{F}\Psi_r$ in (6) and (8), FNSISTRA is the same as the original FISTA.

The **for** loop in Fig. 3 requires only N complex memory locations ($\hat{\mathbf{X}}, \hat{\mathbf{D}}^k$ are counted outside the loop and $\hat{\mathbf{H}}_{ri}$ and $\hat{\mathbf{H}}_i$ are not included in the calculations as done for FISTA). Thus, the minimum memory requirement of FNSISTRA is $6N + 1$ complex memory locations. The memory requirement for $\hat{\mathbf{H}}_{ri}$ can be reduced by evaluating them from $\hat{\mathbf{H}}_i$ and $\hat{\mathbf{G}}$, and storing $\hat{\mathbf{G}}$ instead.

III. EXPERIMENTAL RESULTS

For testing the performance of the proposed approach we used the ShearLab 3D software implementation of the DNST [16] based on [17], [18] with the default shearlet filters with 4, 4, 8 and 8 directional filters for scales $j = 0, 1, 2$ and 3, producing $I = 25$ subbands. We found experimentally that the value $L = 8$ is a reasonable choice. An alternative to such an approach is the use of backtracking, as explained in [13], but this significantly increases the modified algorithm complexity. In all the experiments with FNSISTRA we used $\lambda = 7.5 \cdot 10^{-4}$ (except in the last experiment) and $K = 50$ iterations as a stopping criterion. To evaluate the performance of FNSISTRA we used four different 256×256 MRI images shown in Fig. 4(a)–(d). We carried out all the experiments using Matlab 2010b on a HP desktop with Intel i3-2100 3.1 GHz processor. The reconstruction time for FNSISTRA was approximately 14s. We compared the performance of the proposed approach represented by FNSISTRA with four other approaches represented by the algorithms: RecPF [9], FCSA [15], both obtained from [19], TGVSHCS [7] obtained from [20] and FICOTA [14] implementation based on [14], [21]. Since RecPF and FCSA iterations are faster, to obtain reconstruction times comparable to FNSISTRA, for them we used 350 iterations as a stopping criterion. For similar reasons we used 65 iterations for FICOTA. For TGVSHCS we used 50 iterations resulting in a reconstruction time of 38s. To obtain good average reconstruction performance we searched for near optimal values of the different parameters in each of the algorithms. We compared the approaches using different subsampling ratios, defined as $M/N \cdot 100[\%]$, and two different subsampling types: the random variable density subsampling from [15], [19] and the radial subsampling from [9], [19]. Examples of the two subsampling types are shown in Fig. 4(e)–(f). The performance comparison is shown in Figs. 5 and 6, measured in terms of the $SNR = 10 \log_{10} \frac{\|\mathbf{x}\|_2^2}{\|\mathbf{x} - \mathbf{x}^K\|_2^2}$, where \mathbf{x}^K is the vectorized reconstructed image after the K -th iteration and \mathbf{x} is the vectorized original image.

FNSISTRA shows the best performance within the considered subsampling ratio range with all images. The amount of performance improvement obtained with FNSISTRA depends on the subsampling type used and on the image type. The good performance of the proposed approach is due to three reasons: the excellent spatial localization properties and directional selectivity of DNST, the acceleration in (14), and the projections in (12) and (13). The performance improvement due to the projections comes from the use of additional information about the structure of \mathbf{x} . The improvement due to using DNST compared to using contourlet transform is observed by comparing

$$\begin{aligned} \hat{\mathbf{D}}^k &= \mathcal{F}\Psi_r \mathbf{u}^k = \sum_{i=1}^I \hat{\mathbf{H}}_{ri} \odot \hat{\mathbf{U}}_i^k = \sum_{i=1}^I \hat{\mathbf{H}}_{ri} \odot \left(\hat{\mathbf{R}}_i^k - \frac{1}{L} \hat{\mathbf{H}}_{ri}^* \odot \left(\mathcal{F}\Phi^H \Phi (\Psi_r \mathbf{r}^k) \right) + \frac{1}{L} \hat{\mathbf{H}}_{ri}^* \odot \left(\mathcal{F}\Phi^H \mathbf{y} \right) \right) \\ &\stackrel{(a)}{=} \sum_{i=1}^I \hat{\mathbf{H}}_{ri} \odot \left(\hat{\mathbf{R}}_i^k - \frac{1}{L} \hat{\mathbf{H}}_{ri}^* \odot \mathbf{M} \odot \left(\mathcal{F}\Psi_r \mathbf{r}^k \right) + \frac{1}{L} \hat{\mathbf{H}}_{ri}^* \odot \hat{\mathbf{Y}} \right) \\ &\stackrel{(b)}{=} \sum_{i=1}^I \hat{\mathbf{H}}_{ri} \odot \hat{\mathbf{R}}_i^k - \frac{1}{L} \sum_{i=1}^I \hat{\mathbf{H}}_{ri} \odot \hat{\mathbf{H}}_{ri}^* \odot \mathbf{M} \odot \left(\sum_{i=1}^I \hat{\mathbf{H}}_{ri} \odot \hat{\mathbf{R}}_i^k \right) + \frac{1}{L} \sum_{i=1}^I \hat{\mathbf{H}}_{ri} \odot \hat{\mathbf{H}}_{ri}^* \odot \hat{\mathbf{Y}} \\ &\stackrel{(c)}{=} \hat{\mathbf{B}}^k - \frac{1}{L} \hat{\mathbf{B}}^k \odot \mathbf{M} \odot \hat{\mathbf{G}} + \frac{1}{L} \hat{\mathbf{Y}} \odot \hat{\mathbf{G}} \end{aligned} \quad (9)$$

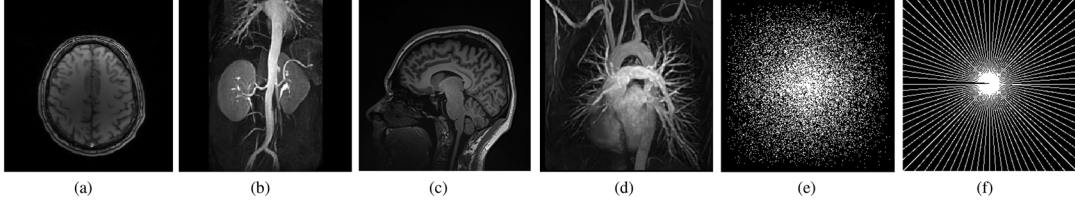


Fig. 4. (a)-(d) The images used to test the performance of FNSISTRA, (e) random variable density subsampling with subsampling ratio 20.5% (f) radial subsampling with subsampling ratio 18.8%. (a) Image 1 (b) Image 2 (c) Image 3 (d) Image 4 (e) Subsampling 1 (f) Subsampling 2.

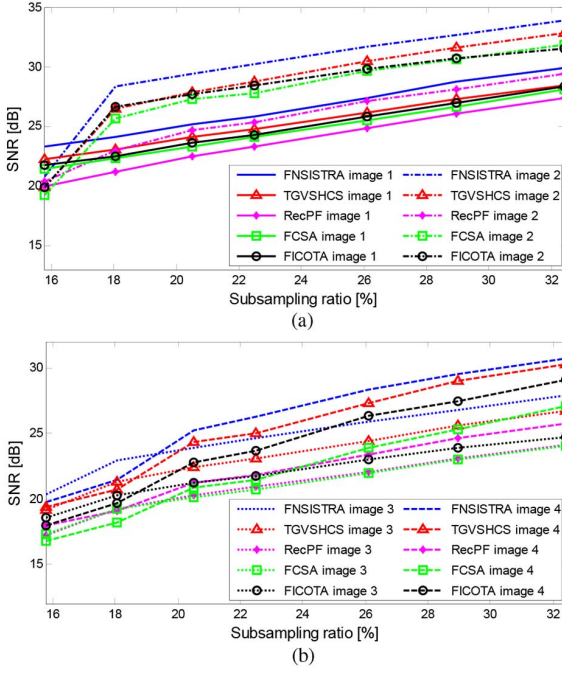


Fig. 5. The reconstruction performance of different approaches with random variable density subsampling using the images from Fig. 4. (a) SNR vs. subsampling ratio for images 1 and 2 (b) SNR vs. subsampling ratio for images 3 and 4.

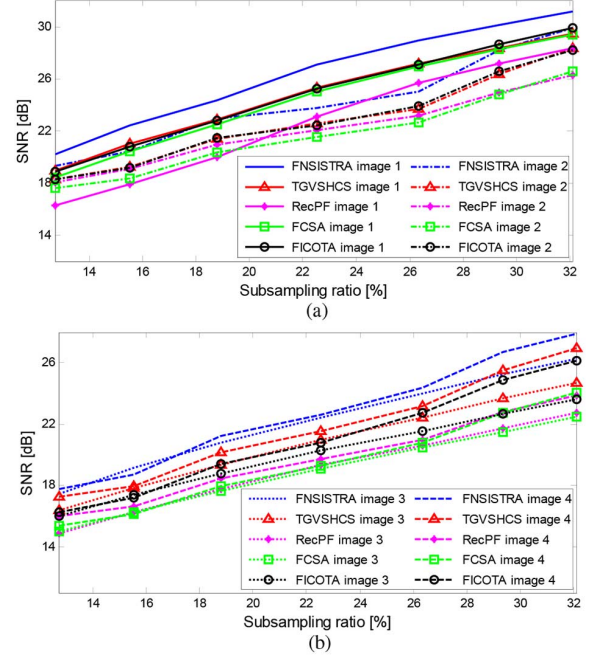


Fig. 6. The reconstruction performance of different approaches with radial subsampling using the images from Fig. 4. (a) SNR vs. subsampling ratio for images 1 and 2. (b) SNR vs. subsampling ratio for images 3 and 4.

FNSISTRA and FICOTA simulation results. Fig. 7 shows the contribution of the acceleration in (14), and the projections in (12) and (13) using image 1 from Fig. 4(a) with variable density random subsampling and a subsampling ratio 20.5%. From Fig. 7, using (14) leads to a peak increase of more than 3 dB compared to the case when the acceleration in (14) and the projections in (12) and (13) are not used. The projections lead to an additional 1.4 dB peak increase, and substantially extend the region of λ/L for high reconstruction quality. This shows the approach robustness to the choice of λ , which is desirable in practice, since the true image is unknown and λ must be chosen in advance. λ/L should be reduced with the increase of K and M/N .

The complexity of FNSISTRA mostly depends on the number of iterations and the number of filters I . Having precomputed $\hat{\mathbf{H}}_i$, $\hat{\mathbf{H}}_{ri}$, $\frac{1}{L}\hat{\mathbf{Y}} \odot \hat{\mathbf{G}}$, $\mathbf{1} - \frac{1}{L}\mathbf{M} \odot \hat{\mathbf{G}}$, $\frac{\lambda}{L}$ and t^k , for each iteration the algorithm requires $I + 1$ 2D FFT and $I + 1$ 2D IFFT operations, $2NI + 2N$ complex multiplications, $3N + (I - 1)N$ complex additions/subtractions, additional $2IN + 2N$ logical operations and IN real additions/subtractions. The calculation assumes that the thresholding function for real numbers is carried out using two logical operations (comparisons to 0) and a subtraction and that the projection consumes two logical operations. Most of the complexity comes from the 2D FFT and 2D IFFT operations and is proportional to the number of subbands

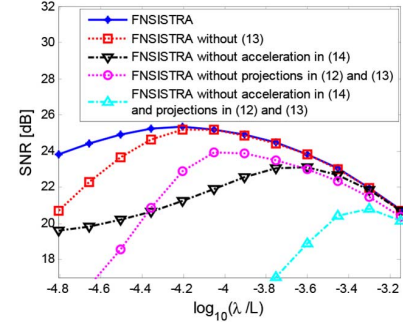


Fig. 7. SNR vs. $\log \lambda/L$ where λ varies and $L = 8$.

I . Thus, the modified algorithm can be speeded up by using parallel processing with multiple cores.

IV. CONCLUSION

We proposed the use of the DNST as a sparsifying transform for compressed sensing MRI and implemented a FISTA based reconstruction algorithm tuned to the DNST. The experimental results showed that the proposed approach outperformed all the other approaches used for comparison (implemented as RecPF, FCSA, TGVSHCS and FICOTA), when comparable execution times were used. The algorithm was much faster than TGVSHCS, but slower than RecPF, FCSA and FICOTA for the same number of iterations.

REFERENCES

- [1] S. Jalali, A. Maleki, and R. Baraniuk, "Minimum complexity pursuit for universal compressed sensing," *IEEE Trans. Inf. Theory*, vol. 60, no. 4, pp. 2253–2268, Apr. 2014.
- [2] C. Qi, G. Yue, L. Wu, and A. Nallanathan, "Pilot design for sparse channel estimation in OFDM-based cognitive radio systems," *IEEE Trans. Veh. Technol.*, vol. 63, no. 2, pp. 982–987, Feb. 2014.
- [3] M. Lustig, D. Donoho, and J. M. Pauly, "Sparse MRI: The application of compressed sensing for rapid MR imaging," *Magn. Reson. Med.*, vol. 58, no. 6, pp. 1182–1195, 2007.
- [4] S. Ravishanker and Y. Bresler, "Sparsifying transform learning for compressed sensing MRI," in *IEEE 10th Int. Symp. Biomedical Imaging*, Apr. 2013, pp. 17–20.
- [5] Y. Hu, G. Ongie, S. Ramani, and M. Jacob, "Generalized higher degree total variation (HDTV) regularization," *IEEE Trans. Image Process.*, vol. 23, no. 6, pp. 2423–2435, Jun. 2014.
- [6] C. Lu and H. Huang, "TV + TV2 regularization with nonconvex sparseness-inducing penalty for image restoration," *Math. Probl. Eng.*, pp. 1–15, Mar. 2014.
- [7] W. Guo, J. Qin, and W. Yin, "A new detail-preserving regularity scheme," Rice CAAM, Tech. Rep. 13-01, 2013.
- [8] J. Aelterman, H. Q. Luong, B. Goossens, A. Pizurica, and W. Philips, "Augmented lagrangian based reconstruction of non-uniformly sub-nyquist sampled MRI data," *Signal Process.*, vol. 91, no. 12, pp. 2731–2742, 2011.
- [9] J. Yang, Y. Zhang, and W. Yin, "A fast alternating direction method for TVL1-L2 signal reconstruction from partial Fourier data," *IEEE J. Select. Topics Signal Process.*, vol. 4, no. 2, pp. 288–297, 2010.
- [10] W.-Q. Lim, "Nonseparable shearlet transform," *IEEE Trans. Image Process.*, vol. 22, no. 5, pp. 2056–2065, 2013.
- [11] W.-Q. Lim, "The discrete shearlet transform: A new directional transform and compactly supported shearlet frames," *IEEE Trans. Image Process.*, vol. 19, no. 5, pp. 1166–1180, May 2010.
- [12] G. Kutyniok, W.-Q. Lim, and X. Zhuang, "Digital shearlet transforms," in *Shearlets: Multiscale Analysis for Multivariate Data*, G. Kutyniok and D. Labate, Eds. Boston, MA, USA: Birkhäuser, 2012, pp. 239–282.
- [13] A. Beck and M. Teboulle, "A fast iterative shrinkage-thresholding algorithm for linear inverse problems," *SIAM J. Imag. Sci.*, vol. 2, no. 1, pp. 183–202, 2009.
- [14] W. Hao, J. Li, X. Qu, and Z. Dong, "Fast iterative contourlet thresholding for compressed sensing MRI," *Electron. Lett.*, vol. 49, no. 19, pp. 1206–1208, Sep. 2013.
- [15] J. Huang, S. Zhang, and D. Metaxas, "Efficient MR image reconstruction for compressed MR imaging," *Med. Image Anal.*, vol. 15, no. 5, pp. 670–679, 2011.
- [16] ShearLab 3D software [Online]. Available: http://www.shearlab.org/index_software.html
- [17] G. Kutyniok, W.-Q. Lim, and R. Reisenhofer, "Shearlab 3D: Faithful digital shearlet transforms based on compactly supported shearlets," *ArXiv:1402.5670*.
- [18] G. Kutyniok, M. Shahram, and X. Zhuang, "Shearlab: A rational design of a digital parabolic scaling algorithm," *SIAM J. Imag. Sci.*, vol. 5, no. 4, pp. 1291–1332, 2012.
- [19] [Online]. Available: http://ranger.uta.edu/~huang/r_lsi.htm
- [20] [Online]. Available: <http://www.math.ucla.edu/~qinjingonly/tgvshcs/>
- [21] X. Qu, W. Zhang, D. Guo, C. Cai, S. Cai, and Z. Chen, "Iterative thresholding compressed sensing MRI based on contourlet transform," *Inv. Probl. Sci. Eng.*, vol. 18, no. 6, pp. 737–758, 2010.